This manuscript has been submitted for publication in *Geophysical Research Letters*. Please note that, despite having gone through peer-review, the manuscript has yet to be formally accepted for publication. Subsequent versions of this manuscript may have slightly different content. If accepted, the final version of this manuscript will be available via the 'Peer-reviewed Publication DOI' link on the right-hand side of this webpage.

Tsunami Early Warning from Global Navigation Satellite System Data using Convolutional Neural Networks

Donsub Rim[1], Robert Baraldi[2*], Christopher M. Liu[3], Randall J. LeVeque[3,4], and Kenjiro Terada[4],

[1]Dept. of Mathematics and Statistics, Washington University in St. Louis, MO, USA
[2]Sandia National Laboratories, Albuquerque, NM, USA
[3]Dept. of Applied Mathematics, University of Washington, Seattle, WA, USA
[4]International Research Institute of Disaster Science, Tohoku University, Aoba-ku, Sendai, Japan

Key Points:

- A deep convolutional neural network is trained to predict tsunami waveforms, based only on GNSS data for hypothetical CSZ earthquakes.
- Less than 9 minutes of data at GNSS stations selected from the existing dense network is used to predict 6 hours of tsunami waveforms.
- Results compare favorably with a previous forecast model based on 30 or 60 minutes of tsunami waveform data.

*This research was sponsored by the Department of Energy Office of Science under the Advanced Scientific Computing Research John von Neumann Fellowship. Sandia National Laboratories is a multimission laboratory managed and operated by National Technology and Engineering Solutions of Sandia, LLC., a wholly owned subsidiary of Honeywell International, Inc., for the U.S. Department of Energy's National Nuclear Security Administration under contract DE-NA0003525. This paper describes objective technical results and analysis. Any subjective views or opinions that might be expressed in the paper do not necessarily represent the views of the U.S. Department of Energy or the United States Government.

Corresponding author: Randall J. LeVeque, `rjl@uw.edu`

Abstract

We investigate the potential of using Global Navigation Satellite System (GNSS) observations to directly forecast full tsunami waveforms in real time. We train convolutional neural networks (CNNs) to use less than 9 minutes of GNSS data to forecast the full tsunami waveforms over 6 hours at select locations, and obtain accurate forecasts on a test dataset. Our training and test data consists of synthetic earthquakes and associated GNSS data generated for the Cascadia Subduction Zone (CSZ) using the MudPy software, and corresponding tsunami waveforms in Puget Sound computed using GeoClaw. We use the same suite of synthetic earthquakes and waveforms as in earlier work where tsunami waveforms were used for forecasting, and provide a comparison. We also explore varying the number of GNSS stations, their locations, and their observation durations.

Plain Language Summary

Producing rapid real-time forecasts for tsunamis in the first few minutes of an earthquake is a challenging problem. Accurate forecasts often rely on direct measurements of the tsunami, which are only available at sparse locations, and only after the tsunami has passed the sensors. Real-time numerical modeling of the tsunami is also time consuming. This work attempts to bypass these difficulties by considering a model that can forecast tsunami wave heights based only on Global Navigation Satellite System (GNSS) data, which is available within minutes from an extensive network of stations. We present some initial results using this approach for hypothetical tsunamis originating from the Cascadia Subduction Zone, with forecast locations in Puget Sound. We show that this approach gives comparable results to earlier work based on observing tsunami waveforms for 30 or 60 minutes, but now using only a few minutes of GNSS data. We explore varying the number of GNSS stations and find that the model yields accurate forecasts when as few as 20 GNSS stations are used, and outperforms our previous model when additional stations are used. The model performs well even when only the initial 4 minutes of GNSS data is used.

1 Introduction

Accurate tsunami early warning allows for more effective emergency planning, thereby mitigating the human and economic toll. However, constructing a rapid forecast model is challenging for several reasons. One is that the underlying physical processes are governed by partial differential equations whose solution requires substantial computation that cannot be performed in a short timeframe. Furthermore, determining the proper initial conditions for the differential equations requires solving the earthquake source inversion problem, which itself holds significant uncertainty due to the lack of direct observations. The current US warning system relies on early estimates of earthquake location and magnitude from seismic data, coupled with direct tsunami observations from DART sensors (Deep Ocean Assessment and Reporting of Tsunamis, (Titov et al., 2005)) in the deep ocean and coastal tide gauges. The sparsity of such sensors limits the amount of data one can collect on the tsunami directly. Moreover, one has to wait for the tsunami to reach these sensors, which can be hours after the earthquake.

In previous work (Liu et al., 2021a), hereafter referred to as Liu21, we explored machine learning (ML) techniques to forecast tsunami waveforms at two "forecast gauges" in the Puget Sound (denoted Gauges 901 and 911) shown in Figure 1. The forecasts were based on synthetic tsunami observations from Cascadia Subduction Zone (CSZ) events at an hypothetical "observation gauge" (denoted Gauge 702) in the Strait of Juan de Fuca. This ML approach avoids the need for real-time source inversion and tsunami simulation. We showed that several hours of tsunami waveforms at the forecast gauges could be forecast from shorter time series at the observation gauge, but it still requires 30–60 minutes of observed data after the tsunami reaches the observation gauge.

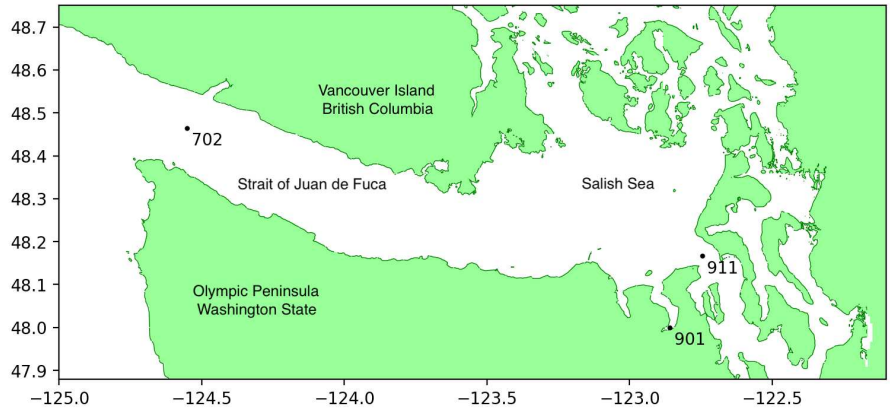

Figure 1. Strait of Juan de Fuca (SJdF) region with gauge locations. Gauge 702 is the hypothetical observation gauge used in Liu21, while Gauge 901 in Discovery Bay and 911 in Admiralty Inlet are the forecast gauges used both in that work and here. Reprinted with permission from (Liu et al., 2021a).

In this paper, we show that equally good forecasts can be made using only a few minutes of data from an existing network of Global Navigation Satellite System (GNSS) stations. Tsunami warning centers are already starting to incorporate this data in performing earthquake magnitude estimates, and it has been shown that the use of GNSS data can have great benefits, particularly for near-field forecasting (Crowell et al., 2018; Melgar, Allen, et al., 2016; Ohno et al., 2022; Ohta et al., 2018; Williamson et al., 2020). We show that this can be taken further by training Convolutional Neural Networks (CNNs) to forecast the tsunami waveforms directly from the GNSS waveforms. Recently ML has been applied to GNSS data in other approaches to tsunami warning, e.g. to produce a model that rapidly estimates the earthquake magnitude (Lin et al., 2021), or as a supplement to ocean pressure sensor data to improve tsunami forecasts (Makinoshima et al., 2021; Tsushima et al., 2014). But to our knowledge this is the first demonstration of the potential for very rapid forecasting of accurate tsunami waveforms based only on a few minutes of GNSS data.

We consider the same forecast Gauges 901 and 911 as in Liu21, and use the same set of 959 CSZ events to train and test the ML model. In contrast to Liu21, our model input is now less than 9 minutes of GNSS data from a set of up to 60 GNSS stations (selected from a set of 62 stations shown in Figure 2). We show that this model does as well as the Liu21 model, despite using observation data that is available almost immediately after the earthquake. Moreover, all 62 GNSS stations exist in practice (along with many more in the CSZ region), and there is a similar or greater density of GNSS stations in other active subduction zone regions such as Japan (Kawamoto et al., 2017) and Chile (Báez et al., 2018). Consequently, the methods studied here may be widely applicable to other subduction zones around the world.

2 GNSS and Tsunami Waveform Datasets

The hypothetical earthquakes used for training the ML model are the same as those used in Liu21, which were taken from a set of 1300 synthetic CSZ events that were generated by Melgar, LeVeque, et al. (2016) and archived at (Melgar, 2016), and that range in magnitude from Mw 7.8 to 9.3. These realizations were generated using a Karhunen-Loève (KL) expansion as proposed by LeVeque et al. (2016) and implemented in the fake-

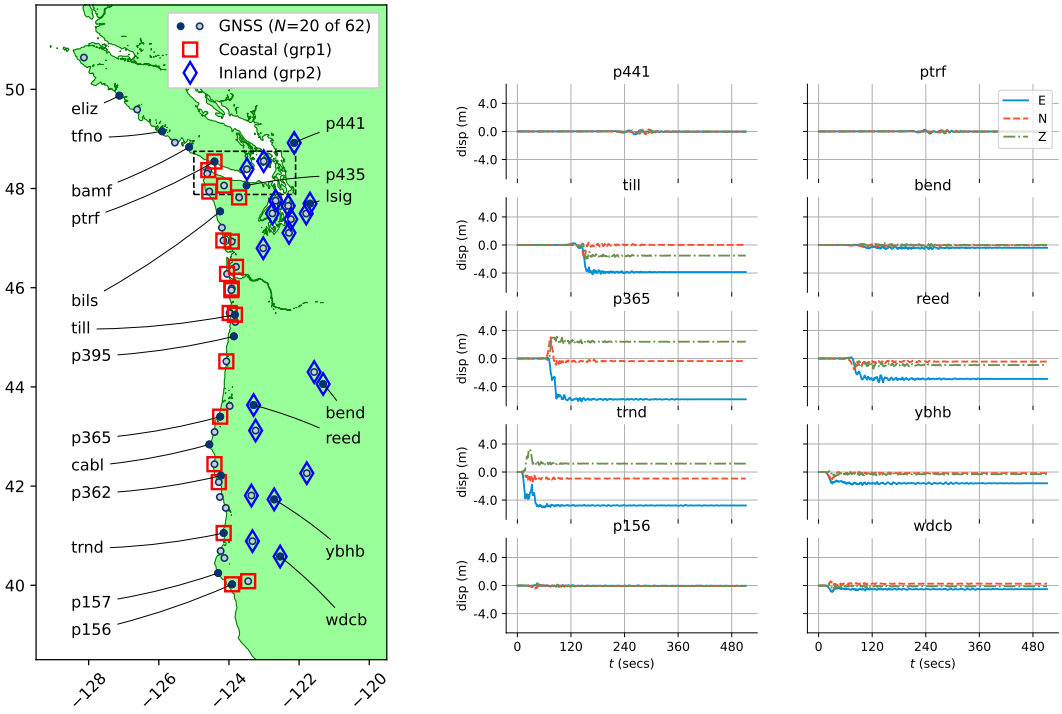

Figure 2. The map shows the location of 62 GNSS stations, with a subset of 20 stations used in the sensor robustness study indicated with labels. The rectangle shows the study area from Figure 1. Sample GNSS data from 10 stations is shown on the right, for one CSZ earthquake Realization #1127. The red and blue symbols show the Group 1 and 2 stations discussed in the text, near the coast and inland, respectively. Up to 512 seconds of GNSS data is used to insure the full signal reaches all stations for all events.

quakes module of the MudPy software (Melgar, 2020). We used the seafloor motion for each event as data for a tsunami simulation, performed using the GeoClaw software (Clawpack Development Team, 2020). Synthetic gauges placed at the gauge locations 702, 901, and 911 recorded the simulated tsunami over a 6 hour period. As in Liu21, from the set of 1300 realizations we chose $N_{\text{data}} = 959$ events with significant tsunamis, and used $N_{\text{train}} = 613$ realizations (64%) in the training set, reserving $N_{\text{valid}} = 154$ and $N_{\text{test}} = 192$ realizations (16% and 20%) for the validation and test sets, respectively. All sets contained a random sample of events from the full range of magnitudes. Further details of the preparation appear in (Text S1).

The main contrast between this work and Liu21 is that our model now only utilizes the synthetic GNSS data from each of the events. This data at the 62 GNSS stations was computed with MudPy and archived at (Melgar, 2016); the original paper using this data focused on the use of GNSS data in the context of earthquake early warning.

Figure 2 shows the location of the 62 stations and a typical set of 20 stations chosen for training a model in our robustness study discussed below. The GNSS data for one sample realization #1127 at 10 of these stations is also shown to illustrate this data. Three channels (E, N, Z) are recorded corresponding to ground motion in the east, north, and vertical direction, respectively. For plots of the slip, seafloor deformation, and tsunami propagation for this same realization #1127, see Liu21.

3 Methods

3.1 Forecast Model

Our forecast model is an ensemble of convolutional neural networks(CNNs). Each CNN has an input variable of dimension $N_{\text{gnss}} \times N_{\text{dir}} \times N_{\text{in}}$ and output variable of dimension $N_{\text{gauge}} \times N_{\text{out}}$. Here, N_{gnss} denotes the number of GNSS stations used for prediction, $N_{\text{dir}} = 3$ the number of GNSS channels (E, N, Z), N_{in} the number of data points in the GNSS measurements (with a sampling rate of 1 Hz), $N_{\text{gauge}} = 3$, the total number of gauges where we make the forecast of the surface elevation, $N_{\text{out}} = 256$ the number of data points in computed tsunami surface elevation (tsunami waveform) over 6 hours. In our experiments, the choice of stations and N_{gnss} will be varied. To vary the number of seconds of observations used, we keep N_{in} fixed and mask the later values.

The CNN first applies a sequence of 9 pairs of convolutional and max-pool layers, then applies the 8 transposed convolutional layers (Goodfellow et al., 2016). The CNN model is implemented and trained using the framework provided in the Python package `pytorch` (Paszke et al., 2019). Precise specifications of the model appear in Text S2.

3.2 Model Training

Our goal is to estimate the parameters of the CNNs by solving a standard optimization problem: with GNSS data as input, we minimize the L_1 error function between the CNN output and free surface time series as a function of the CNN parameters (Goodfellow et al., 2016); the L_1 error tends to prioritize larger magnitude events. In this minimization process, we can train the CNN by finding the parameters that best fit the data. This optimization is done using the stochastic gradient descent algorithm Adam (Kingma & Ba, 2015) with batch size 20 and fixed learning rate 10^{-4}. Rather than training a single CNN, we will train an ensemble made up of 25 CNNs. For each ensemble, we train CNNs individually via Adam until the validation error reaches a certain threshold.

3.3 Experiments

We perform three experiments. First, we conduct a sensor robustness study to explore the performance of the trained ensemble with respect to the number of GNSS stations used. We train 6 separate ensembles, with the number of GNSS stations used for input taken as $N_{\text{gnss}} = 10, 20, \ldots, 60$. We randomly select a non-clustered subset of stations for each N_{gnss} (e.g. see Figure 2, full list in Table S1).

Second, we test how the observation duration affects the forecast performance. We vary the amount of GNSS data used by masking the input values after specified times $T_{\text{gnss}} = 120,\ 240,\ 360$ or $480s$. When varying the observation duration, we use $N_{\text{gnss}} = 60$ stations throughout.

Third, we examine the effect that the sensor's distance to the fault may have on the performance. Among the GNSS stations south of 49° latitude we select two groups of $N_{\text{gnss}} = 20$ stations: Group 1 stations lie along the coast, Group 2 farther inland (as shown in Figure 2).

4 Results

We carry out the training procedure using NVIDIA Tesla V100 SXM2 32GB and it typically takes 90 minutes to complete training one ensemble. We provide the full details regarding the training in the supporting plots in Figures S1 and S2.

Selected forecast waveforms from the test set are shown in Figure 3 for the ensemble $N_{\text{gnss}} = 60$. For comparison, we include the predictions by the model developed in Liu21 based on 60 minutes of tsunami observation data from Gauge 702. The prediction error for Gauge 901 is expected to be higher than for 911 because of its location in Discovery Bay. The shallower 901 location corresponds to larger waves with more nonlinear behavior than the deeper water at Gauge 911. Figure 3 also shows Taylor diagrams (Taylor, 2001) summarizing the forecast results for both the other CNN ensembles that we trained in our robustness study ($N_{\text{gnss}} = 10, \ldots, 60$), as well as those from Liu21. Taylor diagrams give a way of visualizing three measures of similarity between different time series, and have been used for this purpose in some other tsunami modeling studies, e.g. (Lu et al., 2013). From these figures, we gather that the GNSS model exploiting input from all 60 stations performed the best.

Although the CNNs were trained using the L_1 error function, we additionally measure the skill of the CNN ensembles in predicting the maximum surface elevation $\eta_{\max}$ at each gauge, a primary quantity of interest in judging the magnitude of the tsunami at each location. To predict $\eta_{\max}$, we simply compute the maximum of the forecast waveform of each individual model in the ensemble and use the mean as the predicted value. Plots demonstrating the forecast performance $\eta_{\max}$ are shown in Figures 4–5.

Figure 4 shows a plot of the mean absolute error and maximum absolute error, along with the L_1 test error for each ensemble. The L_1 test error and the error metrics for $\eta_{\max}$ follow similar trends. Figure 5 shows scatter plots of the forecast $\eta_{\max}$ vs. the observed value (i.e., the value from the GeoClaw simulation) for each event in the test set. In general, both small and large tsunamis are forecast accurately. Also note that there are large magnitude events that created relatively small tsunamis at the gauge locations considered, and these are also predicted accurately. In the dataset used for these comparisons with Liu21, we filtered out events for which the tsunami signal was below a threshold, as described above. However, we obtain similar results when the model is trained and tested using the full unfiltered dataset, as shown in (Text S3).

For the CNN ensembles trained in the sensor robustness study, the performance generally improves when more GNSS stations are used, but relatively little improvement

of overall performance is seen beyond 20 stations and this threshold agrees with the change in the decay behavior of the validation error. The sharpest decline in the performance of the model occurs when only 10 stations are used.

When 30 or more stations are used, we see increased overall performance of the CNNs trained with GNSS data than those reported in Liu21. This illustrates important practical advantages of using the GNSS data: we obtain a highly accurate forecast with data available within 9 minutes from the start of the tsunamigenic earthquake event, as opposed to 60 minutes after the tsunami starts to enter the Strait as required in Liu21, potentially a 2-hour difference. Moreover, these GNSS stations actually exist and are operational. This makes the new model a more suitable candidate for use in an early warning system.

The ensembles using varying observation durations show that the performance is not significantly affected when only the first 240s of GNSS data is used, suggesting that accurate forecast is possible within 4 minutes. The duration required for other locations will naturally depend on the distance from the fault to the GNSS stations and the duration of the earthquake events of interest. However, in general this duration will be on the order of minutes rather than the hours often require to obtain direct tsunami observations. This also implies that the model relies on seismic waves that propagate some time after the event away from the fault.

The results from ensembles using two different groups of 20 stations show that using only the stations that are situated inland at a significant distance from the fault causes the performance to deteriorate, especially for larger events (Figure 5). This suggests the model relies significantly on the measurements closer to the fault. But also note that both perform worse than when an equal number of well-distributed stations are used ($N_{\text{gnss}} = 20$). A sensitivity study using projected gradients supports these findings (Text S4).

5 Conclusions

We have developed a CNN model that uses less than 9 minutes of GNSS observations at existing onshore stations near the CSZ to produce a 6-hour forecast of the resulting tsunami waveforms at several gauge locations. These gauge locations agree with those used in our previous work denoted Liu21 (Liu et al., 2021a). We demonstrate that this GNSS-based approach works as well as our previous model input of 30 or 60 minutes of the tsunami waveform observed at a hypothetical gauge. We conclude that this approach is very promising for use in real-time warning systems and deserves further development.

Several aspects of our work require additional research that is currently underway. We chose gauge locations in Puget Sound, WA for our study in Liu21 with the idea that observations at a single gauge (e.g. our Gauge 702) at the entrance of the Strait of Juan de Fuca might be sufficient to produce good forecasts in Puget Sound. That was important since there are currently no suitable observation gauges in this region and deploying even one gauge would be expensive. In this work, we used the same gauge locations in order to compare forecasts with our previous results; however, the existence of numerous GNSS stations in the region warrants further exploration of our model's ability to train and generate forecasts at other locations. We are currently collaborating with researchers at the NOAA Center for Tsunami Research to explore the ability of these ML models to provide both nearfield warnings for a CSZ event and also to potentially complement the existing farfield forecasting capabilities based on DART data. In addition to further experiments based on CSZ events, we are working with other researchers at Tohoku University to experiment with forecasting Nankai Trough events.

Our tests have all been performed so far with the synthetic GNSS data produced by the fakequakes software, without the addition of any noise. Real GNSS data can be

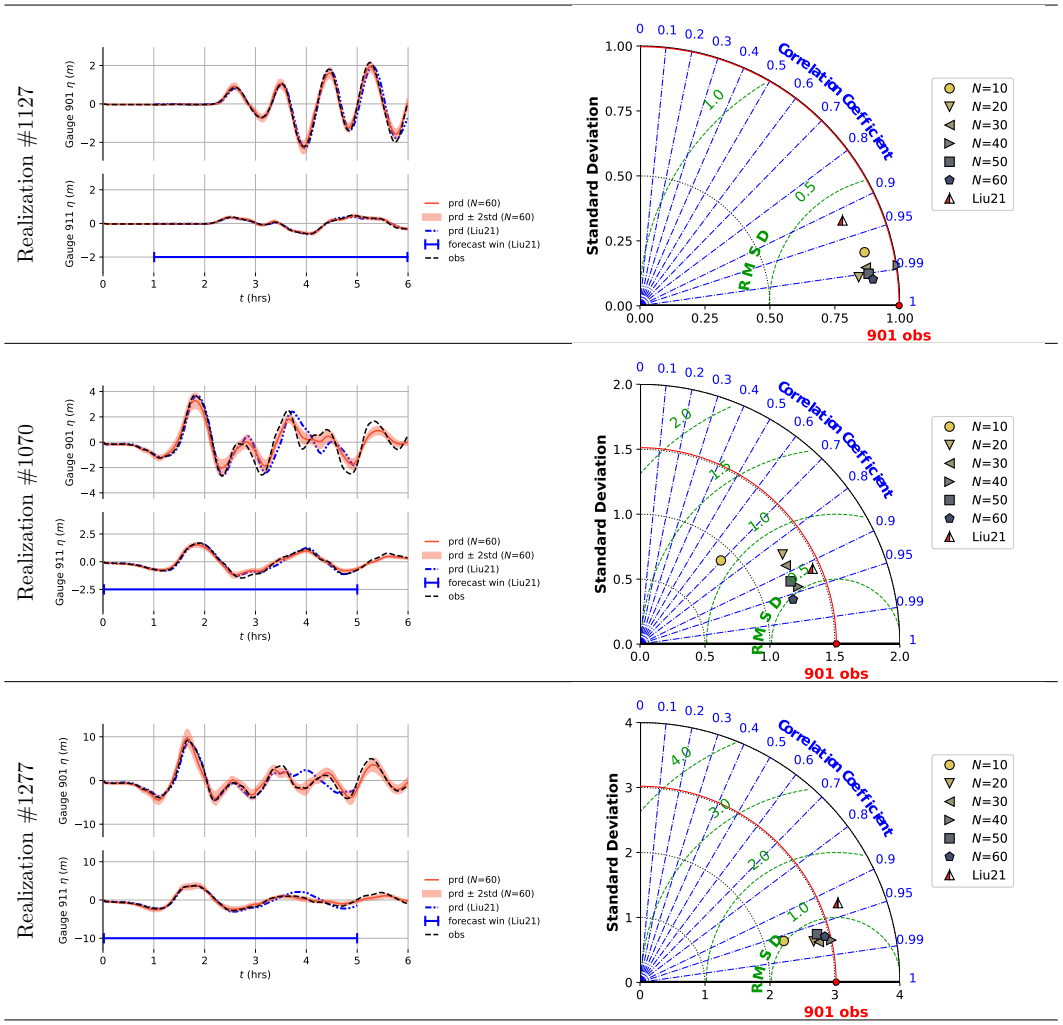

Figure 3. The left column shows time series forecasts using the ensemble $N_{\text{gnss}} = 60$ for gauge locations 901 and 911 for three sample realizations. The top realization (#1127) was also illustrated in Liu21. The right column shows the Taylor diagram for each realizations for gauge 901, now comparing the results obtained using 7 different ML predictions. Six of these use a varying number of GNSS stations N_{gnss} from 10 to 60, while the point denoted by "Liu21" is the previous result for the 5-hour forecast window from Liu21, that used 60 minutes of tsunami waveform from Gauge 702 as input data. The Taylor diagram (e.g. (Taylor, 2001; Lu et al., 2013)) simultaneously shows the standard deviation of each waveform separately (radial distance), the RMS error relative to the correct waveform (green contours), and the correlation coefficient between the forecast and correct waveforms (angular distance, blue contours). More accurate forecasts give points closer to the red dot.

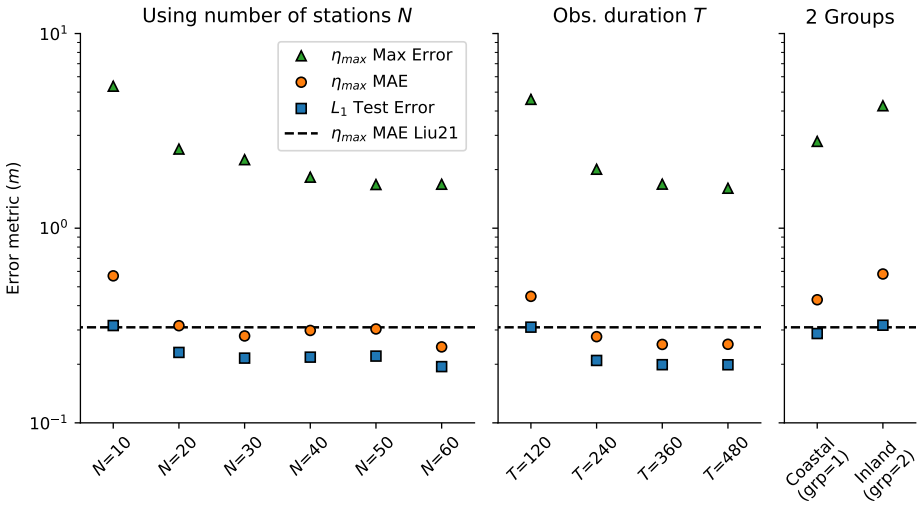

Figure 4. Model performance measured by comparing the maximum surface elevation $\eta_{\max}$ in the forecast waveform to that of the correct waveform, for each realization in the test set. The mean absolute error (MAE) and maximum error, as well as the L_1 test error are plotted. The MAE for model in Liu21 is also shown. Overall best result is obtained using all stations $N_{\text{gnss}} = 60$ and all 512 seconds of GNSS data.

quite noisy and it will be important to assess the robustness of this ML approach to noisy data. The synthetic GNSS waveforms are based on a simplified model of the earth's structure; we plan to explore how robust our CNN model is to synthetic data produced with a different model of the earth. This acts as a step towards exploring how well a model trained on synthetic data would forecast a real tsunami when the input data is from actual GNSS observations.

6 Open Research

The software for all numerical experiments performed in this work is available at `https://github.com/dsrim/ML_GNSS_SJdF_2022` under the BSD-3 license. The earthquake realizations used in this paper were generated by Melgar, LeVeque, et al. (2016) and archived at (Melgar, 2016). The tsunami waveforms for each realizations were generated using the GeoClaw Software (Clawpack Development Team, 2020), and available at (Liu et al., 2021b).

Acknowledgments

Diego Melgar generated the hypothetical earthquakes used in this work and provided advice on the best use of GNSS data. The authors are also grateful to Xinsheng Qin for setting up and performing the GeoClaw simulations used as training and test data. Responding to the comments and questions of two anonymous referees led to significant improvements in this paper. RJL and CML were supported in part by Tohoku University.

References

Báez, J. C., Leyton, F., Troncoso, C., del Campo, F., Bevis, M., Vigny, C., ... Blume, F. (2018). The Chilean GNSS network: Current status and progress toward early warning applications. *Seismological Research Letters*, *89*, 1546–

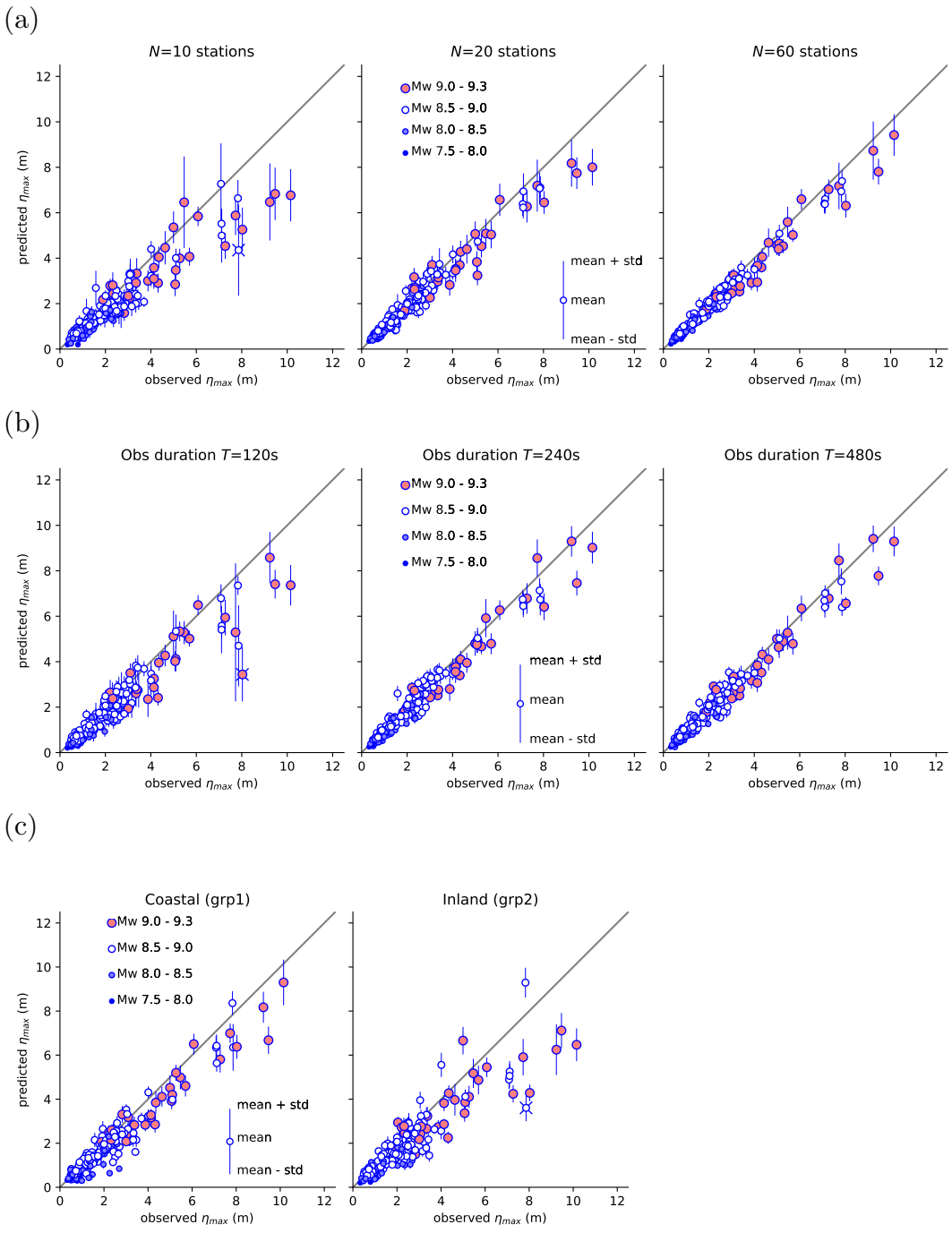

Figure 5. The scatter plots of the predicted $\eta_{\max}$ (the maximum surface elevation at the gauge 901 over the full time series) versus the correct value for each realization in the test set, for ensembles trained on (a) $N_{\text{gnss}} = 10$, 20, 60 stations, (b) observation durations $T_{\text{gnss}} = 120$, 240, 480s, (c) the two stations groups. In each row the prediction with worst error is marked by $\times$, and sensitivity studies for these cases appear in SI (Text S4).

1554. doi: 10.1785/0220180011

Clawpack Development Team. (2020). *Clawpack software.* Retrieved from `http://www.clawpack.org` doi: 10.17605/osf.io/kmw6h

Crowell, B. W., Melgar, D., & Geng, J. (2018). Hypothetical real-time GNSS modeling of the 2016 Mw 7.8 Kaikoura Earthquake: Perspectives from ground motion and tsunami inundation prediction. *Bulletin of the Seismological Society of America*, *108*, 1736–1745. doi: 10.1785/0120170247

Goodfellow, I., Bengio, Y., & Courville, A. (2016). *Deep learning.* MIT Press. Retrieved from `http://www.deeplearningbook.org`

Kawamoto, S., Ohta, Y., Hiyama, Y., Todoriki, M., Nishimura, T., Furuya, T., ... Miyagawa, K. (2017). REGARD: A new GNSS-based real-time finite fault modeling system for GEONET. *Journal of Geophysical Research: Solid Earth*, *122*, 1324–1349. doi: 10.1002/2016JB013485

Kingma, D. P., & Ba, J. (2015). Adam: A method for stochastic optimization. In *International Conference for Learning Representations.* Retrieved from `http://arxiv.org/abs/1412.6980`

LeVeque, R. J., Waagan, K., González, F. I., Rim, D., & Lin, G. (2016). Generating random earthquake events for probabilistic tsunami hazard assessment. *Pure and Applied Geophysics*. doi: 10.1007/s00024-016-1357-1

Lin, J.-T., Melgar, D., Thomas, A. M., & Searcy, J. (2021). Early warning for great earthquakes from characterization of crustal deformation patterns with deep learning. *Journal of Geophysical Research: Solid Earth*, *126*, e2021JB022703. doi: 10.1029/2021JB022703

Liu, C. M., Rim, D., Baraldi, R., & LeVeque, R. J. (2021a). Comparison of machine learning approaches for tsunami forecasting from sparse observations. *Pure and Applied Geophysics*, *178*(12), 5129–5153. doi: 10.1007/s00024-021-02841-9

Liu, C. M., Rim, D., Baraldi, R., & LeVeque, R. J. (2021b). *Comparison of machine learning approaches for tsunami forecasting from sparse observations [data sets]* [dataset]. `http://faculty.washington.edu/rjl/pubs/MLSJdF2021`. doi: 10.5281/zenodo.5156748

Lu, W., Jiang, Y., & Lin, J. (2013). Modeling Propagation of 2011 Honshu Tsunami. *Engineering Applications of Computational Fluid Mechanics*, *7*, 507–518. Retrieved from `https://doi.org/10.1080/19942060.2013.11015489` doi: 10.1080/19942060.2013.11015489

Makinoshima, F., Oishi, Y., Yamazaki, T., Furumura, T., & Imamura, F. (2021). Early forecasting of tsunami inundation from tsunami and geodetic observation data with convolutional neural networks. *Nature Communications*, *12*, 2253. doi: 10.1038/s41467-021-22348-0

Melgar, D. (2016). *Cascadia FakeQuakes waveform data and scenario plots [Data set]. Journal of Geophysical Research.* [dataset]. `http://doi.org/10.5281/zenodo.59943`.

Melgar, D. (2020). *Mudpy.* Retrieved from `https://github.com/dmelgarm/MudPy` doi: 10.5281/zenodo.3703200

Melgar, D., Allen, R. M., Riquelme, S., Geng, J., Bravo, F., Baez, J. C., ... Smalley, R. (2016). Local tsunami warnings: Perspectives from recent large events. *Geophys. Res. Let.*, *43*(3), 2015GL067100. doi: 10.1002/2015GL067100

Melgar, D., LeVeque, R. J., Dreger, D. S., & Allen, R. M. (2016). Kinematic rupture scenarios and synthetic displacement data: An example application to the Cascadia Subduction Zone. *Journal of Geophysical Research: Solid Earth*, *121*, 6658-6674.

Ohno, K., Ohta, Y., Hino, R., Koshimura, S., Musa, A., Abe, T., & Kobayashi, H. (2022). Rapid and quantitative uncertainty estimation of coseismic slip distribution for large interplate earthquakes using real-time GNSS data and its application to tsunami inundation prediction. *Earth, Planets and Space*, *74*. doi: 10.1186/s40623-022-01586-6

Ohta, Y., Inoue, T., Koshimura, S., Kawamoto, S., & Hino, R. (2018). Role of real-time GNSS in near-field tsunami forecasting. *Journal of Disaster Research*, *13*, 453–459. doi: 10.20965/jdr.2018.p0453

Paszke, A., Gross, S., Massa, F., Lerer, A., Bradbury, J., Chanan, G., ... Chintala, S. (2019). Pytorch: An imperative style, high-performance deep learning library. In H. Wallach, H. Larochelle, A. Beygelzimer, F. d'Alché Buc, E. Fox, & R. Garnett (Eds.), *Advances in Neural Information Processing Systems 32* (pp. 8024–8035). Curran Associates, Inc.

Selvaraju, R. R., Cogswell, M., Das, A., Vedantam, R., Parikh, D., & Batra, D. (2017, Oct). Grad-CAM: Visual Explanations From Deep Networks via Gradient-Based Localization. In *Proceedings of the IEEE International Conference on Computer Vision (ICCV)*.

Taylor, K. E. (2001). Summarizing multiple aspects of model performance in a single diagram. *Journal of Geophysical Research: Atmospheres*, *106*, 7183–7192. doi: 10.1029/2000JD900719

Titov, V. V., Gonzalez, F. I., Bernard, E. N., Eble, M. C., Mofjeld, H. O., Newman, J. C., & Venturato, A. J. (2005). Real-time tsunami forecasting: Challenges and solutions. *Natural Hazards*, *35*(1), 35–41.

Tsushima, H., Hino, R., Ohta, Y., Iinuma, T., & Miura, S. (2014). tFISH/RAPiD: Rapid improvement of near-field tsunami forecasting based on offshore tsunami data by incorporating onshore GNSS data. *Geophysical Research Letters*, *41*, 3390–3397. doi: 10.1002/2014GL059863

Williamson, A. L., Melgar, D., Crowell, B. W., Arcas, D., Melbourne, T. I., Wei, Y., & Kwong, K. (2020). Toward Near-Field Tsunami Forecasting Along the Cascadia Subduction Zone Using Rapid GNSS Source Models. *Journal of Geophysical Research: Solid Earth*, *125*, e2020JB019636. doi: 10.1029/2020JB019636

Supporting Information for "Tsunami Early Warning from Global Navigation Satellite System Data using Convolutional Neural Networks"

Donsub Rim[1], Robert Baraldi[2], Christopher M. Liu[3], Randall J. LeVeque[3], and Kenjiro Terada[4],

[1]Dept. of Mathematics and Statistics, Washington University in St. Louis, MO, USA

[2]Sandia National Laboratories, Albuquerque, NM, USA

[3]Dept. of Applied Mathematics, University of Washington, Seattle, WA, USA

[4]International Research Institute of Disaster Science, Tohoku University, Aoba-ku, Sendai, Japan

Contents of this file

Text S1. Data Preparation.

For completeness and to make this paper more self-contained, we summarize some of the details of data preparation, quoted directly from Liu21 (Liu et al., 2021). Please refer to that paper for further information.

From the 1300 synthetic events of (Melgar, 2016), we first discarded all realizations for which the resulting tsunami was considered negligible in the region of interest. We exclude from our experiments any realization for which the tsunami surface elevation at Gauge 702 does not exceed 0.1m in amplitude, or where the amplitude at Gauge 901 does not exceed 0.5m during the entirety of simulation time. This reduced the number of realizations from 1300 to 959. We use this same filtering procedure as in Liu21 for a fair comparison of results, but we also trained our CNN ensemble on the unfiltered dataset and obtained similar results (see Text S3).

The time series at each gauge that is output by the GeoClaw tsunami simulation may be at non-uniform times, due to the adaptive mesh refinement algorithms used, so they were interpolated to a uniform set of times with 10 second resolution in order to make equal size datasets from each simulation (comparable to the sampling rate of some instruments).

GeoClaw simulations were performed for each of the 959 realizations over 6 hours of simulated time, with adaptive refinement used to allow refinement to varying resolutions in the computational domain depending on the resolution needed to capture the waves of interest. In Liu21 we then chose a 5-hour forecast window for each event based on the time that the tsunami was first detected at Gauge 702, in the entrance to the Strait. In the present paper we forecast for the full 6-hour tsunami duration based on the GNSS data, but then use the same 5-hour window for each event as in Liu21 when computing error statistics for comparison with that work. In general the forecast is essentially zero for earlier times, so this makes little difference in the errors reported.

Text S2. CNN Architecture.

We specify the architecture of the CNNs used in this work. As mentioned in the paper, the CNN is given an input of size $N_{\text{gnss}} \times N_{\text{dir}} \times N_{\text{in}}$ and first applies a sequence of 9 pairs of convolutional and max-pool layers, then applies the 8 transposed convolutional layers, yielding an output of size $N_{\text{gauge}} \times N_{\text{out}}$. For an introduction to CNNs and the terminology used here, see (Goodfellow et al., 2016). The channel output sizes for each convolutional and transposed convolutional layer are

$$\begin{aligned} \mathbf{C}_{\text{conv}} &= \big(64, \quad 64, \quad 128, \quad 128, \quad 128, \quad 256, \quad 256, \quad 512, \quad 512\big), \\ \mathbf{C}_{\text{tconv}} &= \big(512, \quad 512, \quad 256, \quad 256, \quad 128, \quad 128, \quad 64, \quad 64\big). \end{aligned} \tag{1}$$

Every convolutional layer uses 1D convolutions with kernel size 3, padding size 1, and stride 1, followed by a max pooling of kernel size 2 and stride 2. All transposed convolutional layers use kernel size 2 and stride 2. Between layers, we apply the LeakyReLU activation function with slope 0.5.

Text S3. Unfiltered Dataset Results.

We have additionally trained a CNN ensemble using the dataset that includes the unfiltered 1300 synthetic events with full-length T_{gnss} =512s signals from N_{gnss} =60 GNSS stations. The discarding of negligible events was necessary for a fair comparison with (Liu et al., 2021). However, many events in the dataset had significant GNSS signals but only small-amplitude tsunamis at the gauges in the Strait, and it is interesting to also study whether these events are accurately forecast. This larger dataset is randomly shuffled into the train, validation, and test sets, each of respective sizes 64%, 16%, and 20% of the total dataset.

Figure S3 shows the predicted $\eta_{\max}$ vs. correct for each realization in the test set. We verify that the CNN ensemble performs similarly as it did using the filtered dataset in the

text. In particular, we see that for many large magnitude events the CNN ensemble correctly predict small tsunami amplitudes. This confirms that the discarding of realizations did not significantly affect the overall result.

Text S4. Sensitivity analysis.

As a measure of input sensitivity, we compute the projected gradient of the deep neural network, using as the projection direction the correct signal via back propagation (see, e.g. (Selvaraju et al., 2017)). We computed the gradient with respect to all GNSS input signals located at various stations over all CNNs in an ensemble that used N_{gnss}=20 stations, and plot the mean of the absolute value of the gradients Figures S4-S7 for a few realizations. First, based on the amplitude of the gradient it appears the CNNs utilize the N, Z orientations in the signal more than the E orientation. Second, the figures show that the CNN ensembles are sensitive to 3 time intervals overall, as indicated by the peaks of the gradient amplitudes, which roughly correspond to portions of the signal containing co-seismic deformation, seismic waves, and final displacement. Note that most of the variation in the signal lie in the first 2 intervals. We also plot the realizations where some ensembles performed the worst in Figures S5-S7 and show that in these cases, the input signal is missing some information lying in these intervals of high sentivity that a well-performing ensemble appears to utilize.

References

Goodfellow, I., Bengio, Y., & Courville, A. (2016). *Deep learning*. MIT Press. Retrieved from http://www.deeplearningbook.org

Liu, C. M., Rim, D., Baraldi, R., & LeVeque, R. J. (2021). Comparison of machine learning approaches for tsunami forecasting from sparse observations. *Pure and Applied Geophysics*, *178*(12), 5129–5153. doi: 10.1007/s00024-021-02841-9

Melgar, D. (2016). *Cascadia FakeQuakes waveform data and scenario plots [Data set]. Journal of Geophysical Research.* [dataset]. http://doi.org/10.5281/zenodo.59943.

Selvaraju, R. R., Cogswell, M., Das, A., Vedantam, R., Parikh, D., & Batra, D. (2017, Oct). Grad-CAM: Visual Explanations From Deep Networks via Gradient-Based Localization. In *Proceedings of the IEEE International Conference on Computer Vision (ICCV)*.

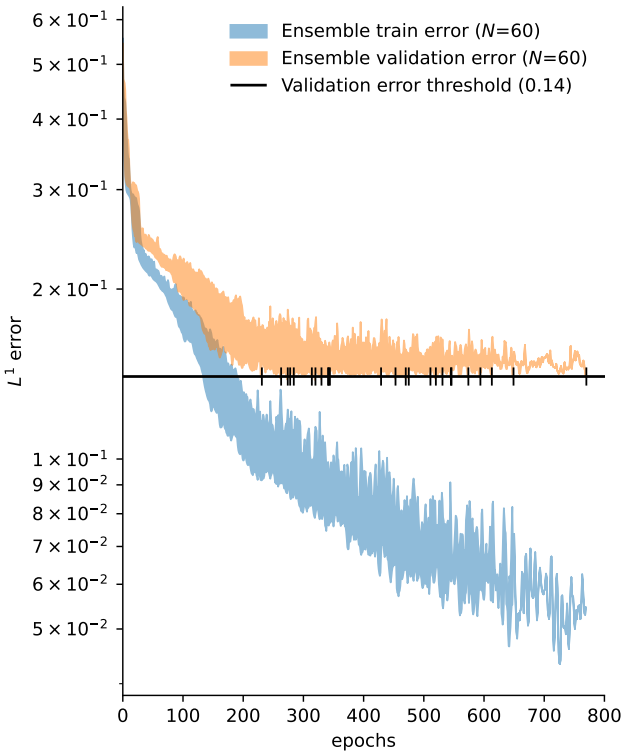

Figure S1. Plot of minimum-maximum range of L_1 training and validation errors at each epoch for the ensemble with $N_{\text{gnss}} = 60$ during the training procedure using stochastic gradient descent algorithm Adam. The validation threshold used for this training is shown as the horizontal line, and the vertical ticks mark the epochs when the validation errors of individual CNNs in the ensemble passed the threshold.

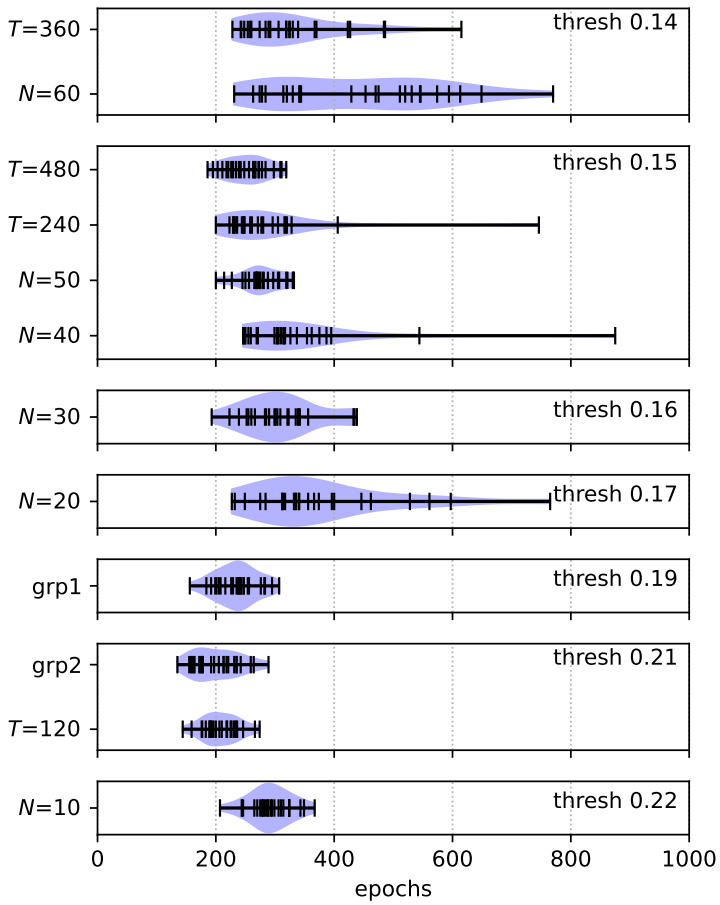

Figure S2. Summary of training result for all ensembles. The y-axis labels indicate the ensemble: $N_{\text{gnss}} = 10, ..., 60$ indicate ensembles with varying number of stations used, $T_{\text{gnss}} = 120, ..., 480$ varying observation durations, `grp1, grp2` the two station groups. We selected the smallest validation threshold achieved among threshold values $0.10, 0.11, 0.12, ..., 0.30$ within 1000 epochs of Adam. For each ensemble made up of 25 CNNs, the epoch when the training error of the individual CNN reached the selected validation threshold is displayed as a tick on the solid horizontal line. We also show a violin plot showing kernel density estimate (sample size 25) of these epochs illustrating their overall distribution. Training was performed on a Intel Xeon Gold 6148 2.4Ghz 20 Core 512GB RAM with NVIDIA Tesla V100 SXM2 32GB over a duration of approximately 90 minutes.

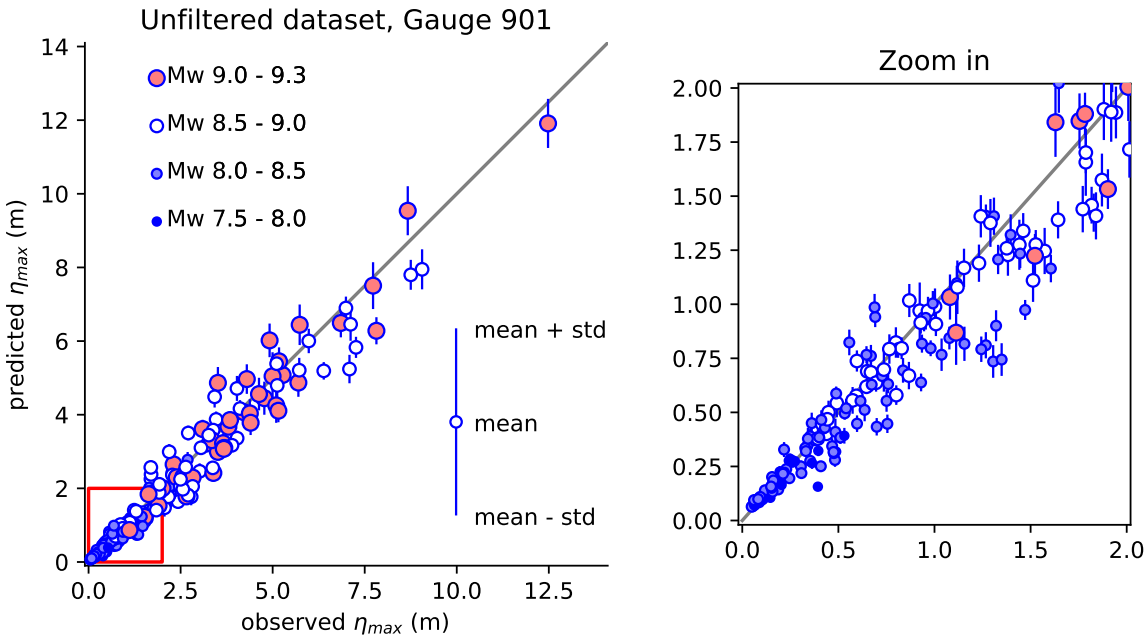

Figure S3. The prediction vs. observation scatter plot for the N_{gnss}=60 ensemble trained on the unfiltered dataset. The predictive performance is similar to that of the ensemble trained on the filtered datset. The Zoom-in plot to the right shows that the CNN ensemble correctly predicts test realizations that were filtered out in the main study, including some large-magnitude events that did not cause significant tsunamis at the synthetic gauges.

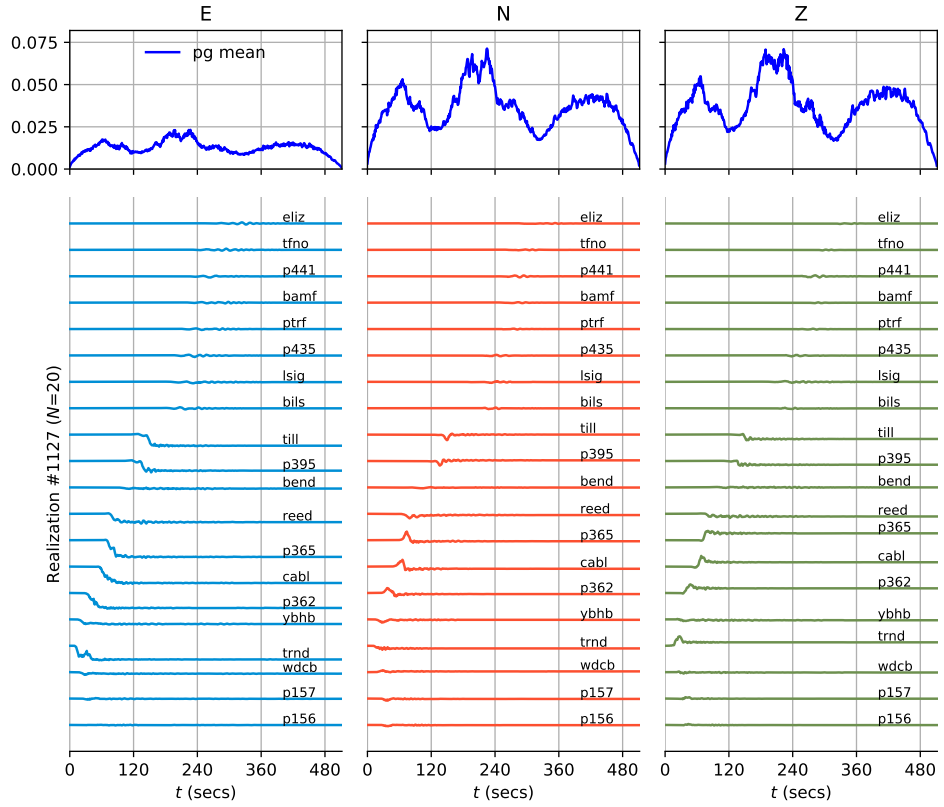

Figure S4. Projected gradient result (top row) and corresponding GNSS input (bottom row) for Realization #1127 and the ensemble $N_{\text{gnss}} = 20$.

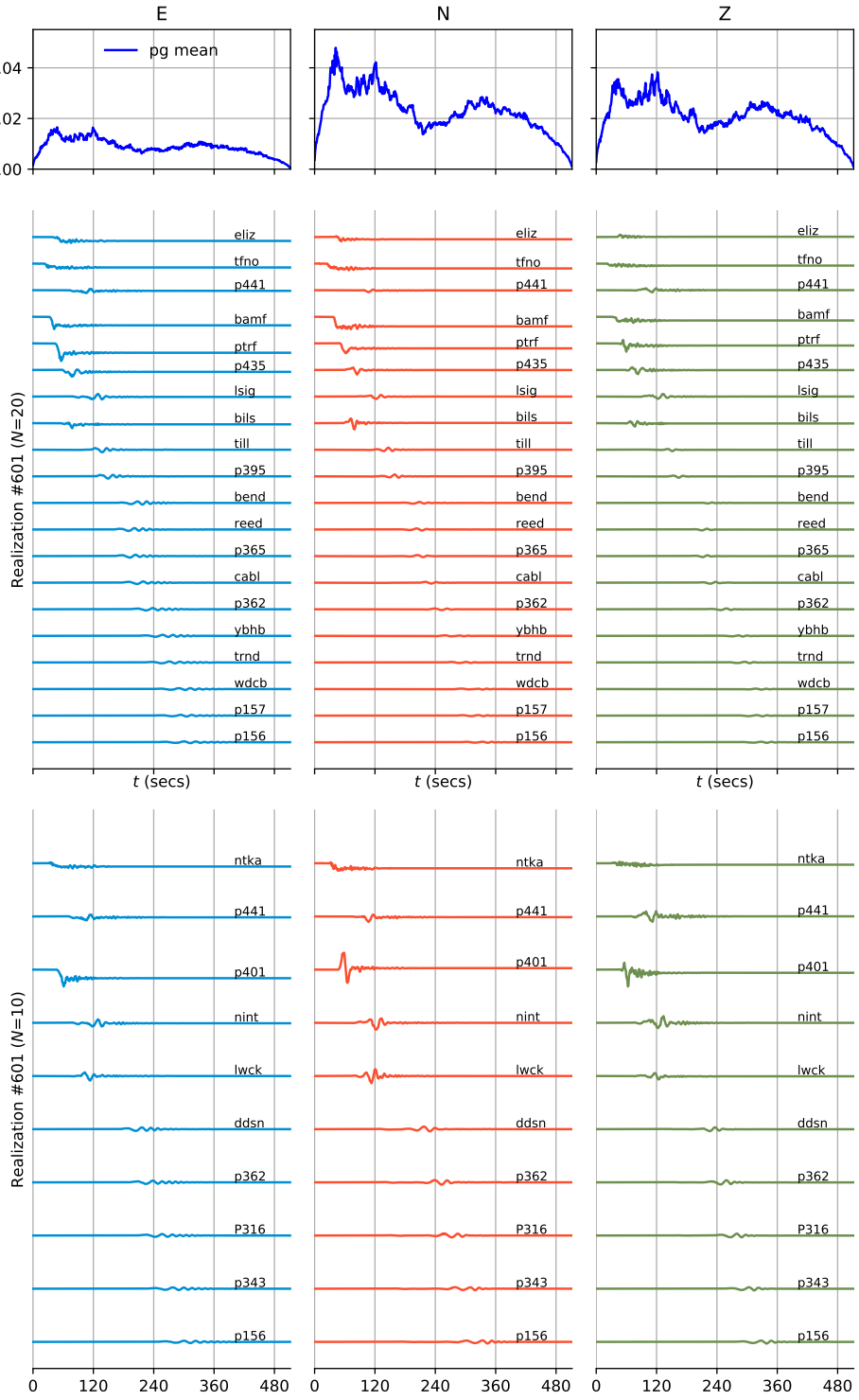

Figure S5. Projected gradient result (top row, see Text S1) and corresponding GNSS input (middle row) for Realization #0601 and the ensemble N_{gnss}=20. GNSS input for the ensemble using fewer stations N_{gnss}=10 (bottom row). The N_{gnss}=10 ensemble prediction for this realization was the worst among the test set (marked by × in Figure 6 (a)), but the N_{gnss}=20 ensemble yielded correct results.

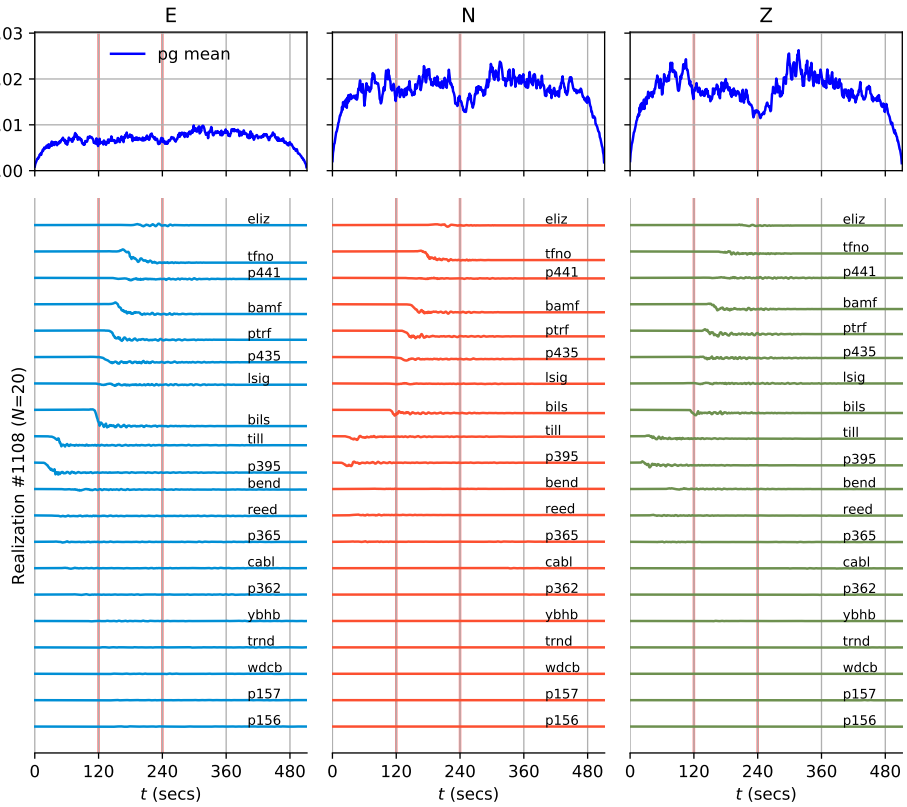

Figure S6. Projected gradient result (top row, see Text S3) and corresponding GNSS input (bottom row) for Realization #1108 and the ensemble N_{gnss}=20. The T_{gnss}=120s ensemble prediction for this realization was the worst among the test set (marked by $\times$ in Figure 6 (b)), but the T_{gnss}=240s ensemble yielded correct results.

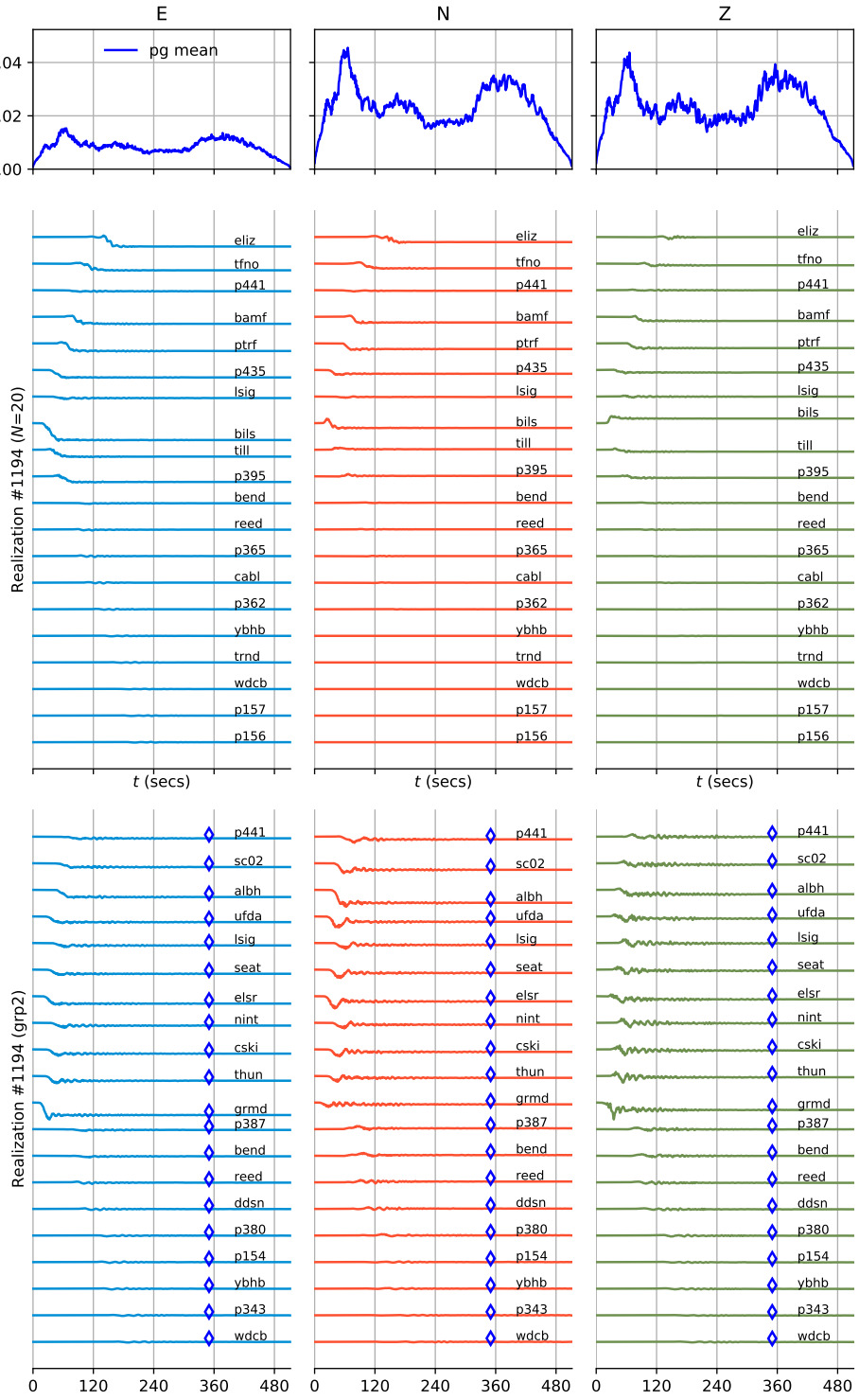

Figure S7. Projected gradient result (top row, see Text S3) and corresponding GNSS input (middle row) for Realization #1194 for the ensemble N_{gnss}=20. GNSS input for the N_{gnss}=20 ensemble (bottom row). The Group 1 ensemble prediction for this realization was the worst among the test set (marked by × in Figure 6 (b)), but the N_{gnss}=20 ensemble yielded correct results.

Table S1. The location of GNSS stations used for input and the group selection for the robustness study N_{gnss}=10, ... , 60.

Station	indicator[a]	longitude	latitude	Station	indicator[a]	longitude	latitude
p156	110111	-123.91	40.02	lwck	101111	-124.05	46.28
p329	000111	-123.45	40.08	p397	001011	-123.80	46.42
p157	010101	-124.31	40.25	grmd	001001	-123.02	46.80
p160	000111	-124.13	40.55	p398	001101	-123.92	46.93
wdcb	011111	-122.54	40.58	ocen	000011	-124.16	46.95
p162	001011	-124.24	40.69	thun	001111	-122.29	47.11
p343	101111	-123.33	40.89	pabh	001101	-124.20	47.21
trnd	010111	-124.15	41.05	cski	001111	-122.24	47.38
P316	101011	-124.09	41.56	oylr	000000	-122.20	47.47
ybhb	010111	-122.71	41.73	nint	100001	-121.80	47.50
ptsg	001011	-124.26	41.78	elsr	000111	-122.76	47.50
p154	000111	-123.36	41.81	bils	010011	-124.25	47.54
p734	001111	-124.29	42.08	seat	001011	-122.31	47.65
p362	110011	-124.23	42.21	lsig	010001	-121.69	47.70
p380	001111	-121.78	42.26	ufda	000111	-122.67	47.76
p733	001111	-124.41	42.44	sc03	000111	-123.71	47.82
cabl	011111	-124.56	42.84	p401	100111	-124.56	47.94
p364	000111	-124.41	43.09	p403	000001	-124.14	48.06
ddsn	100111	-123.24	43.12	p435	011110	-123.50	48.06
p365	011111	-124.25	43.40	neah	001011	-124.62	48.30
p366	000101	-123.98	43.61	mkah	000111	-124.59	48.37
reed	010011	-123.30	43.63	albh	000001	-123.49	48.39
bend	011011	-121.32	44.06	ptrf	011001	-124.41	48.54
p387	000111	-121.57	44.30	sc02	000111	-123.01	48.55
onab	000111	-124.07	44.51	bamf	011111	-125.14	48.84
p395	011111	-123.86	45.02	p441	111111	-122.14	48.92
p396	001111	-123.82	45.31	uclu	000111	-125.54	48.93
till	010011	-123.83	45.45	tfno	010111	-125.91	49.15
chzz	001111	-123.98	45.49	ntka	100001	-126.62	49.59
p407	000111	-123.93	45.95	eliz	011111	-127.12	49.87
seas	001011	-123.92	45.98	holb	001011	-128.13	50.64

[a] The 6-bit array indicates the 6 groups $N_{\text{gnss}} = 10, ..., 60$ the station belongs to.